5

APPLICATION OF THE CONTROL REGION APPROXIMATION TO TWO-DIMENSIONAL ELECTROMAGNETIC SCATTERING

B. J. McCartin, L. J. Bahrmasel and G. Meltz

5.1 Introduction

The scattering of electromagnetic waves by geometrically complex objects is a very interesting theoretical problem that has important implications for many applications. This problem has traditionally been treated either by approximate methods such as the geometric theory of diffraction [1] or by "exact" methods such as integral equation formulations [2]. The approximate methods have the advantage that they are very efficient yet they ignore some basic scattering mechanisms such as travelling waves. The integral equation methods such as the moment method incorporate such contributors but at the price of being very computationally intensive for large, complicated scatterers. In this paper, we propose a numerical method of solution which incorporates a

complete physical model yet ultimately is capable of efficiently treating large, complex three dimensional targets. Herein, we present the two dimensional algorithm.

The basic idea is to bring to bear numerical methods that have proved powerful in such areas as fluid dynamics and solid mechanics. Thus, two dimensional scattering is first formulated as an exterior boundary value problem, which in both the transverse magnetic and transverse electric cases involves a generalized Helmholtz equation. This formulation easily permits complex scatterers composed of lossy dielectric and magnetic materials. Also, thin coatings are readily treated by a surface impedance boundary condition.

Asymptotic boundary conditions are applied [3,4], thus allowing a truncation of the computational domain at a finite distance. Two of the more popular candidates are compared on a model problem. The prospect of using higher order boundary conditions is assessed with the negative conclusion that this is not practicable. An a posteriori method to assess the accuracy of these approximate boundary conditions is suggested.

With these formulational issues aside, attention is next focused on discretizing the boundary value problem. The Control Region Approximation, originally developed for compressible aerodynamic [5] calculations and subsequently extended for semiconductor device simulation [6], is suitably modified for and applied to our scattering problem [7]. In this method, an arbitrary set of discrete points, at which the field will be approximated, is chosen. Each such point is then surrounded by a control region (Dirichlet region). The conservation form of the Helmholtz equation is then enforced on each control region. This involves the numerical approximation of field flux through the control region boundary. The approximation is very easily achieved by utilizing an orthogonality property (duality) of the Dirichlet and Delaunay tessellations [8].

The assembly of the discrete equations, one for each mesh point, results in a coefficient matrix of extremely sparse structure. Thus, the highly developed sparse direct methods [9] may be applied allowing the efficient calculation of monostatic cross sections. In addition to the geometric flexibility offered by the arbitrariness of mesh point locations, a number of other significant benefits are accrued from this method. Because the continuous equation is expressed in conservation form prior to discretization, there is a corresponding discrete conservation law which avoids the local sources and sinks which can appear

in finite element discretizations [10]. This conservation form also guarantees enforcement of appropriate interface conditions between layers. The flux balance nature of this discretization naturally accommodates both the impedance boundary condition along the scatterer and the asymptotic radiation condition along the outer computational boundary. The scheme is second order accurate in smooth regions. Second order accuracy is preserved at corners by appropriate treatment of the singularities present. The accuracy is further enhanced by replacing the traditional polynomial basis functions by alternative trigonometric basis functions.

The solution of the discrete equations is accomplished using the Yale Sparse Matrix Package (YSMP) [11] and relevant features of this package are summarized. Also included are details of the postprocessing calculation of the scattering cross section since in many contexts this is the parameter of primary interest. Finally, a collection of test cases for canonical geometries is presented which illustrate the capabilities of this method. The numerical results are concluded by the comparison of our calculated results with actual test data on a very complex configuration. These results clearly indicate the worth of two dimensional simulation for this problem. The necessary extensions of this technique required to provide fully three dimensional simulation are considered.

5.2 Problem Formulation

Consider the scattering of a two-dimensional electromagnetic wave by a cylindrical obstacle of arbitrary cross-section (Fig. 1). The general solution of such a problem can be obtained by the superposition of Transverse Magnetic (TM) and Transverse Electric (TE) components [12] where

$$\overline{E} = \begin{bmatrix} 0 \\ 0 \\ E_z(x,y) \end{bmatrix}; \quad \overline{H} = \begin{bmatrix} H_x(x,y) \\ H_y(x,y) \\ 0 \end{bmatrix} \quad \text{(TM Case)} \qquad \text{(1a)}$$

$$\overline{E} = \begin{bmatrix} E_x(x,y) \\ E_y(x,y) \\ 0 \end{bmatrix}; \quad \overline{H} = \begin{bmatrix} 0 \\ 0 \\ H_z(x,y) \end{bmatrix} \quad \text{(TE Case)} \qquad \text{(1b)}$$

In the above, we have assumed a harmonic time dependence

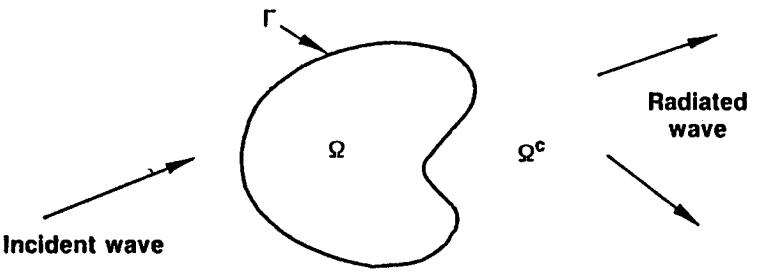

Figure 1 Problem formulation.

$$\tilde{E}(\bar{r},t) = Re\{e^{j\omega t}\overline{E}(\bar{r})\}$$

$$\tilde{H}(\bar{r},t) = Re\{e^{j\omega t}\overline{H}(\bar{r})\} \tag{2}$$

where $(\tilde{E},\tilde{H})$ is the physical field and $(\overline{E},\overline{H})$ is the phasor field.

Upon substitution into Maxwell's equations we obtain the generalized Helmholtz equation

$$\nabla_t \cdot (a\nabla_t u) + bu = 0 \tag{3}$$

where ∇_t is the transverse gradient and

$$u = E_z,\ a = 1/\mu,\ b = \omega^2\epsilon \quad \text{(TM Case)} \tag{4a}$$

$$u = H_z,\ a = 1/\epsilon,\ b = \omega^2\mu \quad \text{(TE Case)} \tag{4b}$$

and ϵ and μ are the complex permittivity and permeability, respectively, each of which may be arbitrary functions of position. Thus, the problem has been reduced to the solution of scalar Helmholtz equations.

These equations must be supplemented by appropriate boundary conditions at the surface of any conductors. In particular, we wish to incorporate the impedance boundary condition [13]

$$\overline{E} - (\overline{E}\cdot\hat{n})\hat{n} = \eta_S\hat{n}\times\overline{H} \tag{5}$$

where η_S is the surface impedance. This condition reduces to

$$\frac{\partial u}{\partial n} + \gamma u = 0 \tag{6}$$

where

$$\gamma = \begin{cases} -\jmath\dfrac{\omega\mu}{\eta_S} & \text{(TM Case)} \\ +\jmath\omega\epsilon\eta_S & \text{(TE Case)} \end{cases} \tag{7}$$

and $\hat{n}$ is the unit normal to the cross-section. Note that $\eta_S = 0$ (perfect conductor) reduces to

$$u = 0 \quad \text{(TM Case)} \tag{8a}$$

$$u_n = 0 \quad \text{(TE Case)} \tag{8b}$$

As it stands, this formulation is not sufficient to guarantee a unique solution. An additional condition is needed to insure that the scattered field is composed of outgoing waves only. Incoming scattered waves are excluded by the Sommerfeld radiation condition

$$\frac{\partial u_S}{\partial r} + \jmath\kappa u_S = O(r^{-1/2}); \quad \kappa^2 = \omega^2\mu\epsilon \tag{9}$$

where the total field has been decomposed into the sum of an incident, u_I, and a scattered, u_S, field

$$u = u_I + u_S \tag{10}$$

Thus, the formulation reduces to the following exterior boundary value problem for the scattered field

$$\nabla \cdot (a\nabla u_S) + bu_S = F = -[\nabla \cdot (a\nabla u_I) + bu_I] \text{ in } \Omega \tag{11a}$$

$$\nabla u_S \cdot \hat{n} + \gamma u_S = -[\nabla u_I \cdot \hat{n} + \gamma u_I] \text{ on } \partial\Omega \tag{11b}$$

$$\frac{\partial u_S}{\partial r} + \jmath\kappa u_S = O(r^{-1/2}) \tag{11c}$$

where we have dropped the subscript on the gradient operator. Note that no restrictions are placed upon the form of u_I, e.g. it need not be

a plane wave. Moreover, the sources generating the incident field may be located at infinity or at a finite distance.

5.3 Asymptotic Boundary Conditions

The radiation boundary condition

$$\frac{\partial u_S}{\partial r} + \jmath\kappa u_S = O(r^{-1/2}) \tag{12}$$

is a condition which seemingly must be applied infinitely far from the scatterer. Since we are constrained to solve our boundary value problem in a finite domain, we must replace this far-field condition by a near-field equivalent. This near-field expression is in the form of an integral equation along the outer boundary [14]. Discretization of this equation leads to corresponding full matrix rows thus destroying the sparsity crucial to the efficiency of our approach. Thus, we seek a local differential radiation condition approximating the nonlocal integral condition. Such conditions have received considerable attention in the computational acoustics literature [3,4]. We consider two of these approaches in what follows.

The first asymptotic boundary condition we treat is due to Engquist and Majda [3]; a more elementary presentation is given in [15]. The basic idea is to eliminate reflected waves in the frequency domain. However, this results in a non-rational dispersion relation which yields a pseudodifferential operator rather than a differential operator. Thus, a totally non-reflecting differential boundary condition is not achievable. Instead, Engquist and Majda employ Padé approximants to the dispersion relation and use the corresponding differential operator as an approximation to the Sommerfeld operator. The particular boundary condition of interest is

$$(E-M)_2 : \frac{\partial u_S}{\partial r} = \left(-\jmath\kappa - \frac{1}{2r}\right) u_S + \frac{1}{2\kappa^2 r^2}\left(-\jmath\kappa + \frac{1}{r}\right)\frac{\partial^2 u_S}{\partial \theta^2} \tag{13}$$

The second asymptotic boundary condition we consider is due to Bayliss and Turkel [4]; a more elementary presentation is available in [16]. In this method, the scattered field is expanded in an asymptotic series of outgoing waves. The coefficients in the local boundary operator are then obtained by annihilating successive terms in this expansion. The particular boundary condition of interest is

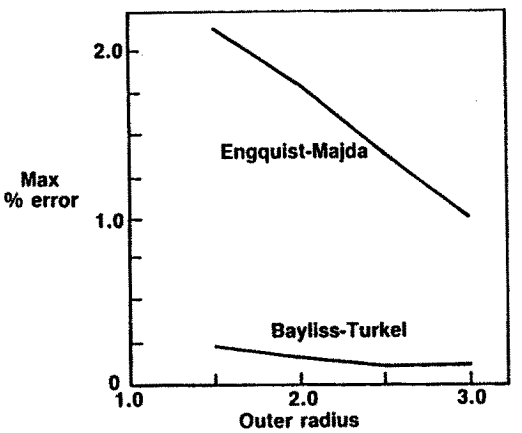

Figure 2 Comparison of boundary conditions.

$(B-T)_2$:

$$\frac{\partial u_S}{\partial r} = \frac{1}{1-\jmath/\kappa r}\cdot\left[\left(-\jmath\kappa - \frac{3}{2r} + \frac{3\jmath}{8\kappa r^2}\right)u_S - \frac{\jmath}{2\kappa r^2}\frac{\partial^2 u_S}{\partial\theta^2}\right] \tag{14}$$

Note that both of these boundary conditions asymptotically yield the Sommerfeld condition

$$\frac{\partial u_S}{\partial r} = -\jmath\kappa u_S \text{ as } r\to\infty \tag{15}$$

It should also be pointed out that each boundary condition is one member of a whole family of boundary conditions. The particular representative has been selected on the basis of compatibility with the interior Helmholtz equation. The prospects for using higher order boundary conditions will be discussed below.

Let us compare $(E-M)_2$ with $(B-T)_2$ on a model problem. In particular, consider the scattering of a TM wave by a perfectly conducting cylinder of size $\kappa a = 1$. The mesh density is selected so that discretization error is negligble so that any error is primarily due to the approximate nature of the outer boundary condition which is enforced on a circumscribing circle. The maximum percentage field errors are then calculated and compared for various locations of the outer boundary. The result, which is displayed in Fig. 2, indicates a

clear advantage for $(B-T)_2$ in this problem. Clearly, the smaller the computational domain the more efficient the overall computation.

The question naturally arises as to whether we can improve the accuracy by increasing the order of the Bayliss-Turkel operator. Let us address this question in some generality. In general,

$$u_S = \sum_n a_n H_n(\kappa r) e^{jn\theta} \tag{16a}$$

$$\frac{\partial u_S}{\partial r} = \sum_n a_n \kappa H_n'(\kappa r) e^{jn\theta} \tag{16b}$$

so that the impedance of the n-th Fourier mode is $\kappa H_n'(\kappa r)/H_n(\kappa r)$.

At a fixed outer radius, R, we consider rational approximation in the frequency domain

$$\frac{H_n'(\kappa r)}{H_n(\kappa r)} \approx \frac{\alpha_0 + \alpha_1 n + - - - \alpha_i n^i}{\beta_0 + \beta_1 n + - - - + \beta_j n^j} \tag{17}$$

which corresponds in the spatial domain to

$$\begin{aligned} \beta_0 \frac{\partial}{\partial r} u_S + \beta_1 \frac{\partial^2}{\partial r \partial \theta} u_S + - - - + \beta_j \frac{\partial^{j+1}}{\partial r \partial \theta^j} u_S \\ = \kappa \alpha_0 u_S + \alpha_1 \frac{\partial}{\partial \theta} u_S + - - - + \alpha_i \frac{\partial^i}{\partial \theta^i} u_S \end{aligned} \tag{18}$$

If the original rational approximation is good then this boundary condition will provide a good impedance match for the Fourier modes and thus reflections from the outer boundary will be negligible.

The efficiency of higher order boundary conditions is now seen to be governed by how well we can approximate H_n'/H_n by rational functions in the frequency domain. Figures 3a and 3b show the real and imaginary parts, respectively of $H_n'(50)/H_n(50)$ together with u_r/u for $(B-T)_2$. We see that $(B-T)_2$ provides a good match for the real part of the impedance for the first 40 modes while the match for the imaginary part is good only for 20 modes. Suppose that we have a scatterer that has excited 60 modes [17]. Can we construct a rational function providing good impedance matches over the entire spectrum present?

To answer this question we have utilized the IMSL routine IRATCU [18] which constructs the rational weighted Chebyshev approximation of specified degree. By exhaustive search we determined

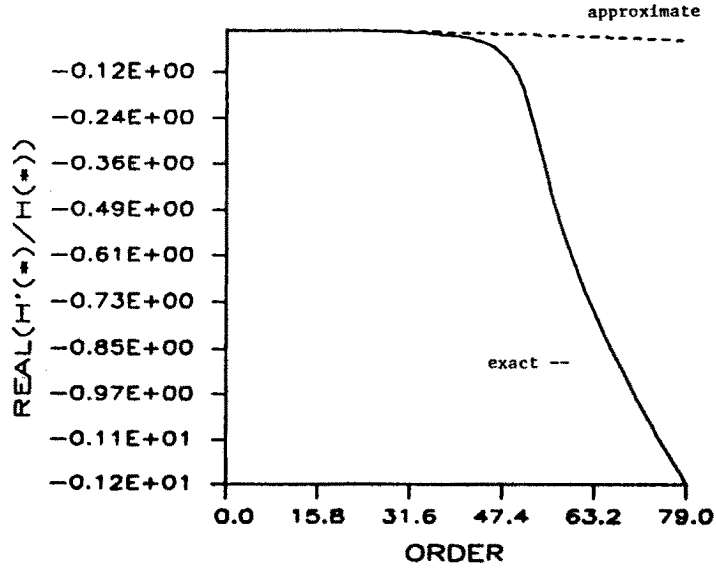

Figure 3a Comparison of Re{Impedence}.

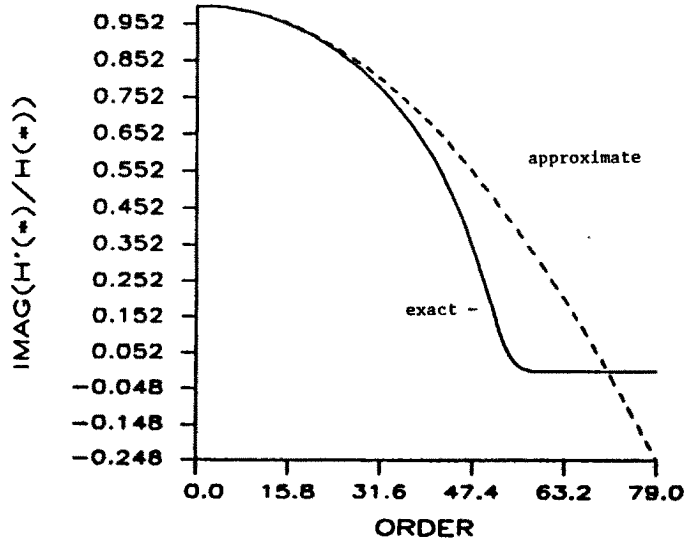

Figure 3b Comparison of Im{Impedence}.

that i = 9, j = 8 for the real part and i = 8, j = 9 for the imaginary part are required to produce good impedance matches for all 60 modes. These approximations are shown in Figs. 4a and 4b.

The high degree of these rational functions in the frequency domain implies a corresponding high degree of the differential operators in the spatial domain. As such, these boundary conditions destroy the very sparsity that they are intended to preserve. This negative result places $(B-T)_2$ in a rather special position; i.e., it is a low order boundary operator that provides good impedance matches for many problems. Yet, to significantly improve upon it requires a vast increase in the order of the boundary condition.

Note that the effectiveness of the asymptotic boundary condition can be assessed *a posteriori* [17] by expanding u_S along Γ in the form

$$u_S \approx \sum_n [a_n H_n^{(1)}(\kappa R) + b_n H_n^{(2)}(\kappa R)] e^{jn\theta} \tag{19}$$

using the calculated values of u_S and $\partial u_S/\partial r$ where

$$\frac{\partial u_S}{\partial R} \approx \sum_n \kappa [a_n H_n^{(1)'}(\kappa R) + b_n H_n^{(2)'}(\kappa R)] e^{jn\theta} \tag{20}$$

Thus, we first employ an FFT to produce

$$u_S = \sum_n A_n e^{jn\theta}, \frac{\partial u_S}{\partial R} = \sum_n B_n e^{jn\theta} \tag{21}$$

and then solve for a_n, b_n as

$$a_n = \frac{\kappa H_n^{(2)'}(\kappa R) A_n - H_n^{(2)}(\kappa R) B_n}{\kappa [H_n^{(1)}(\kappa R) H_n^{(2)'}(\kappa R) - H_n^{(2)}(\kappa R) H_n^{(1)'}(\kappa R)]} \tag{22a}$$

$$b_n = \frac{-\kappa H_n^{(1)'}(\kappa R) A_n + H_n^{(1)}(\kappa R) B_n}{\kappa [H_n^{(1)}(\kappa R) H_n^{(2)'}(\kappa R) - H_n^{(2)}(\kappa R) H_n^{(1)'}(\kappa R)]} \tag{22b}$$

Any nonzero a_n corresponds to a reflected wave from the computational boundary.

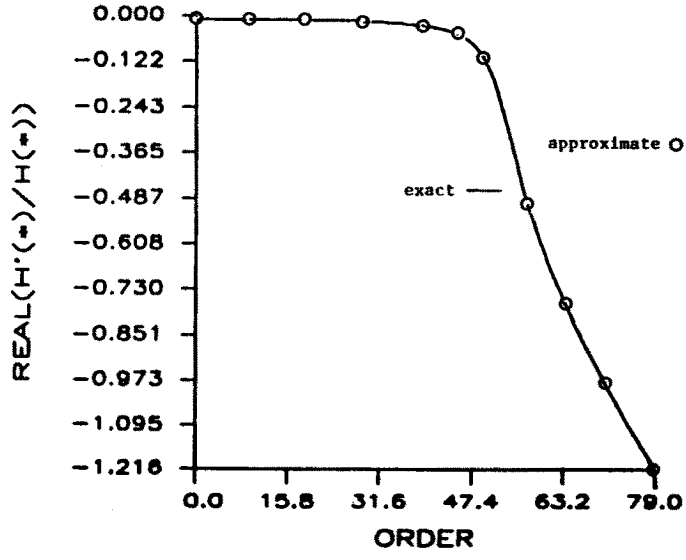

Figure 4a Best rational approximation to Re{Impedence}.

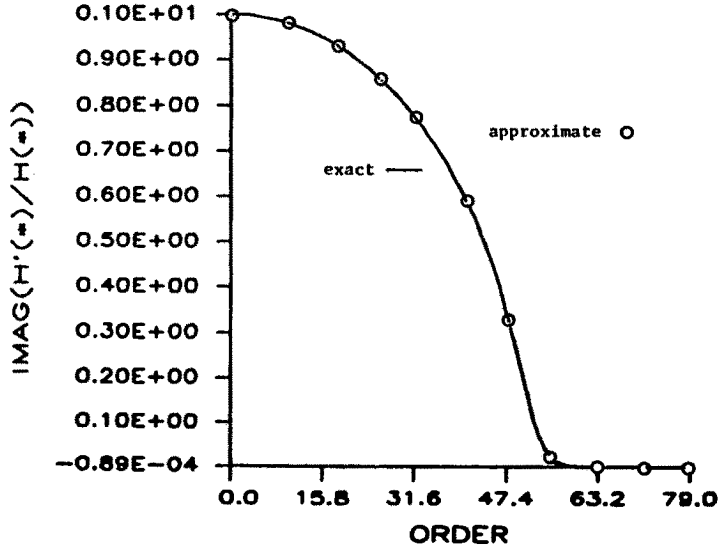

Figure 4b Best rational approximation to Im{Impedence}.

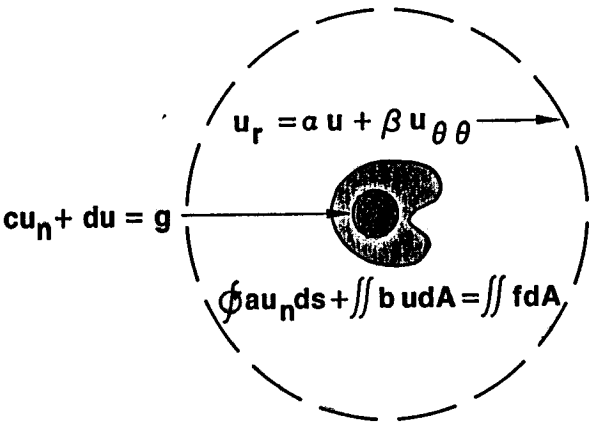

Figure 5 Boundary value problem.

5.4 Discretization

The previous sections have reduced our problem to the solution of the following boundary value problem (Fig. 5)

$$\nabla \cdot (a\nabla u_S) + bu_S = -[\nabla \cdot (a\nabla u_I) + bu_I] \text{ in } \Omega \tag{23a}$$

$$\nabla u_S \cdot \hat{n} + \gamma u_S = -[\nabla u_I \cdot \hat{n} + \gamma u_I] \text{ on } C_i \tag{23b}$$

$$\frac{\partial u_S}{\partial r} + \alpha u_S + \beta \frac{\partial^2 u_S}{\partial \theta^2} = 0 \text{ on } C_0 \tag{23c}$$

In the above, a, b, and γ are (possibly discontinuous) spatially varying complex functions while α and β are complex constants. This continuous formulation must be suitably discretized for computer simulation. Moreover, this discretization must be achieved for arbitrarily shaped scatterers. We effect this discretization via the Control Region Approximation which we now describe.

We first reformulate our problem in integral (conservation) form by integrating over a two-dimensional domain, D, and applying the divergence theorem resulting in

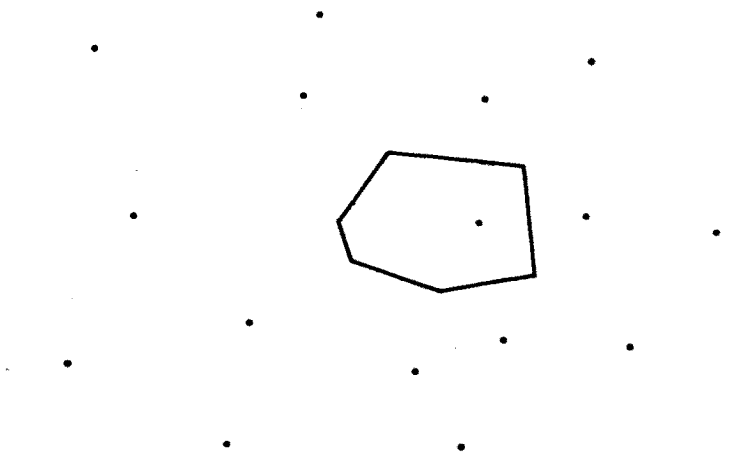

Figure 6a Mesh points.

$$\int_{\partial D} a \frac{\partial u_S}{\partial \nu} d\sigma + \iint_D b u_S \, dA = - \int_{\partial D} a \frac{\partial u_I}{\partial \nu} d\sigma - \iint_D b u_I \, dA \quad (24)$$

The distinct advantage of this reformulation is that it still applies when the coefficients are discontinuous as they typically are in applications involving layered media.

We next select a discrete set of points (grid points, nodal points, etc.,) at which we will approximate the scattered field (Fig. 6a). The rational selection of this point set is, in general, nontrivial and is beyond the purview of this paper. Assuming these points given, we next associate a control region with each point. The control region associated with point P is defined to be the set of all points in the plane closer to P than to any of its neighbors and is known as the Dirichlet region [19] (Fig. 6b) (a.k.a Voronoi region, Thiessen region, Wigner-Seitz cell). The Dirichlet regions are convex polygons whose union is a tessellation of the solution domain known as the Dirichlet tessellation.

The line segments connecting grid points which share an edge of a Dirichlet polygon form a triangulation known as the Delaunay triangulation [20] (Fig. 6c). This triangulation possesses a number of desirable properties relative to finite element discretizations. The Delaunay triangulation is, however, of secondary importance in the present

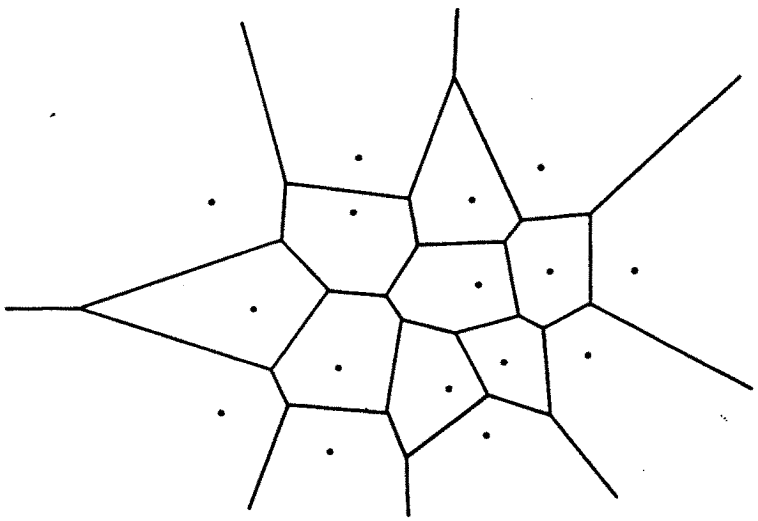

Figure 6b Dirichlet tessellation.

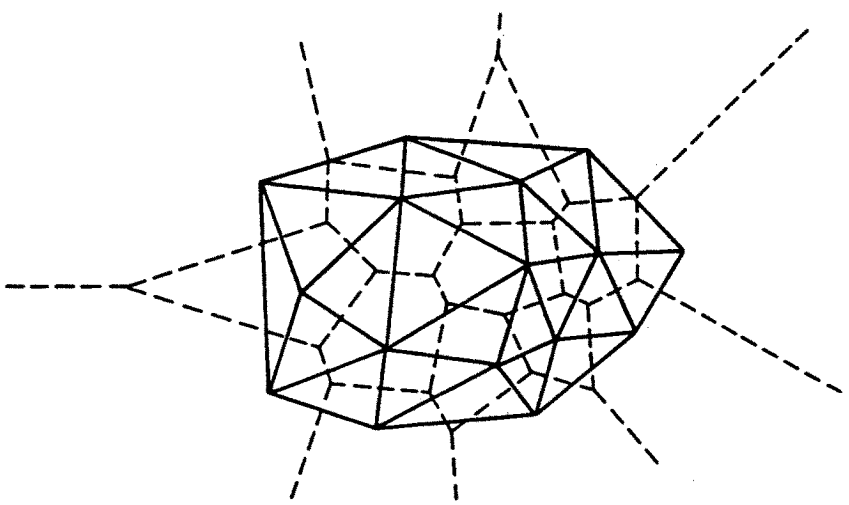

Figure 6c Delaunay tessellation.

method where the Dirichlet tessellation is the fundamental construct. It is important to observe that a Delaunay edge is orthogonal to the corresponding Dirichlet edge. We shall refer to this property as duality. The Delaunay triangles are also used in Watson's method for the construction of the Dirichlet regions [21].

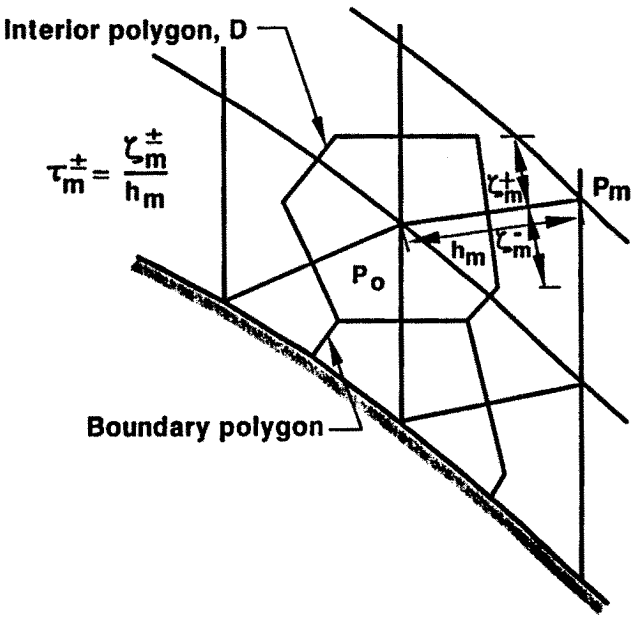

Figure 7 Control region approximation.

We now enforce the conservation form equation upon each control region. After performing the numerical integrations, we arrive at the following discrete equation at point P_0

$$\sum_m (\tau_m^- a_m^- + \tau_m^+ a_m^+)(u_m - u_0) + \sum_m b_{m,0} A_{m,0} u_0 = \sum_m F_{m,0} A_{m,0} \tag{25}$$

where m indexes the polygon sides in Fig. 7. In the above, F represents the source terms due to the incident field and must include appropriate δ-functions along the triangle edges due to discontinuities in a. Note that we have taken advantage of the Dirichlet-Delaunay duality in approximating the normal derivative (flux) terms. It is important to observe that each discrete equation contributes a matrix row which is extremely sparse so that the resulting system can thus be solved very efficiently.

The above difference equation is based upon representing the unknown fields locally by polynomials. However, it is clear that the

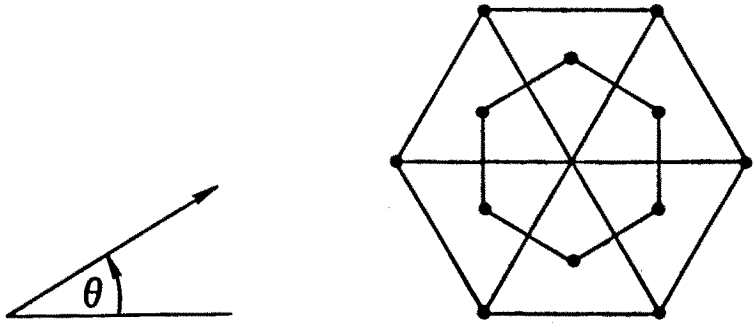

Figure 8a Model problem for alternative basis functions.

solutions we seek are oscillatory and hence are well approximated by polynomials only on fine meshes. This suggests the use of alternative, in this instance trigonometric, basis functions for the local field representation. The use of one-dimensional Green's functions along the triangle edges [22] yields the flux approximation

$$\frac{\partial u_S}{\partial \nu} \approx \frac{\kappa \cos(\kappa \Delta \nu)}{\sin(\kappa \Delta \nu)}(u_m - u_0) \longrightarrow \frac{u_m - u_0}{\Delta \nu} \text{ as } \kappa \Delta \nu \to 0 \qquad (26)$$

In order to compare this approximation to the traditional central difference formula we utilize a model problem. Consider an incident uniform plane wave (Fig. 8a)

$$u_i = e^{j\kappa(x\cos\theta + y\sin\theta)} \qquad (27)$$

impinging upon a regular hexagonal lattice. Placing Dirichlet conditions on the boundary, we then solve for the field at the central point. This provides a measure of the accuracy of the difference approximation versus κh where κ is the wave number and h is the mesh parameter. Figure 8b displays the performance of both the old and new difference schemes. It is readily apparent that applying the alternative basis function representation reduces the error, or what is the same thing, allows the use of a coarser mesh to achieve a fixed level of

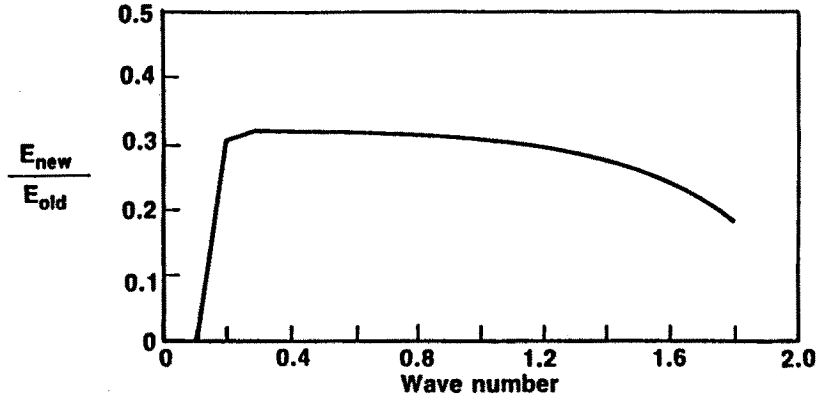

Figure 8b Comparison of absolute error of difference schemes.

resolution. This in turn allows simulation for larger objects with fixed computation time.

The discrete formulation described above must be modified when the scatterer possesses sharp protruding corners. This is due to the singular nature of the derivatives of the field in the neighborhood of such a point [23]. Consider a reentrant corner of exterior measure $\gamma\pi$ (Fig. 9). Locally, the field behaves like

$$u \sim a + b(\theta) r^{1/\alpha} \tag{28}$$

Fitting this form to the unknown fields at the end points of a triangle edge yields

$$u(r,\theta) \sim u_0 + (\bar{u} - u_0)\left(\frac{r}{\bar{r}}\right)^{1/\alpha} \tag{29}$$

and hence

$$u_r\left(\frac{\bar{r}}{2}, \bar{\theta}\right) \sim \frac{\bar{u} - u_0}{\alpha \bar{r}} \tag{30}$$

Some additional observations on the above discretization procedure are in order. The shape of the scatterer is completely arbitrary since the mesh point distribution is essentially unconstrained. Moreover, the material properties may vary continuously, i.e. may be inhomogeneous, or may change abruptly, i.e. may be heterogeneous. Since the governing equation has been written in conservation form, the correct weak solution will be captured in the heterogeneous case without the explicit imposition of jump conditions. Also, the conservation law

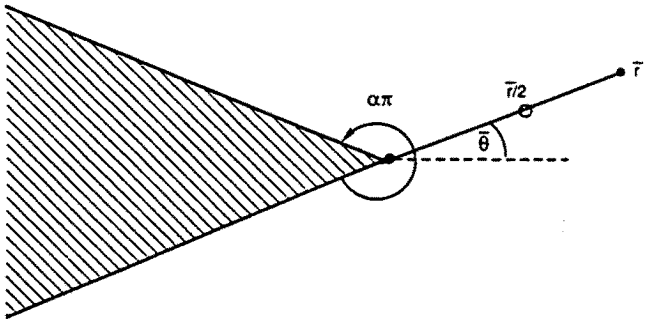

Figure 9 Corner singularity.

itself is preserved in its discrete counterpart, thus avoiding the spurious sources and sinks which can appear in finite element methods. Both the impedance boundary condition and the asymptotic radiation condition involve specification of boundary fluxes and are hence easily incorporated. The scheme as proposed possesses formal second order accuracy which has been preserved by the singularity treatment and enhanced by the inclusion of alternative basis functions. Finally, all the basic ingredients of this technique are extendable to three spatial dimensions as well as to time dependent phenomena.

5.5 Solution of Discrete Equations

The previously described discretization procedure applied to each grid point results in a linear system of equations

$$Au = F \tag{31}$$

where each element of this matrix-vector equation corresponds to a particular point. What is significant here is that the coefficient matrix A is extremely sparse with an average of seven nonzeroes per row (2D) regardless of how many unknowns. This allows the use of the highly developed sparse direct methods which provide efficient solution (both in terms of storage and operation count) of such systems thus allowing simulation of larger objects.

In this work, the Yale Sparse Matrix Package (YSMP) is employed. An LU decomposition is first performed on A, viz.

$$A = LU \tag{32}$$

where L and U are lower and upper triangular, respectively. Then

$$Lv = F \tag{33}$$

is solved by forward substitution followed by solving

$$Uu = v \tag{34}$$

by backward substitution. YSMP provides for automatic reordering of the equations to minimize fill-in during the factorization phase resulting in savings during the subsequent forward and backward substitutions as well as further economizing on storage. An option is also provided for a symbolic LU factorization to precede the numerical LU factorization which reduces execution time if many systems with the same sparsity pattern must be solved. This occurs, for example, when nonlinear materials are treated.

The significance of organizing the computation in this fashion lies in the fact that the LU factorization phase is more costly than the forward/backward substitution phase. If we have many systems with the same coefficient matrix but different righthand sides, we need only do a single factorization thus accruing great savings in computation time. This is precisely the case when we wish to construct the monostatic cross-section since the incident fields appear only in the source terms of the differential equation and boundary conditions. In practice, it has been found that YSMP can handle scatterers up to length 20λ of arbitrary shape and material properties in an engineering workstation computing environment.

5.6 Cross Section Calculation

In many instances, it is a functional of the field, the scattering cross section, rather than the field itself which is of primary interest. Although rightfully a post-processing operation, the scattering cross section is of such importance that we include a discussion of its computation here.

The scattering cross section, $\chi(\theta)$, is defined as the scattered power per unit length in a fixed direction normalized by that of the incident field, i.e.

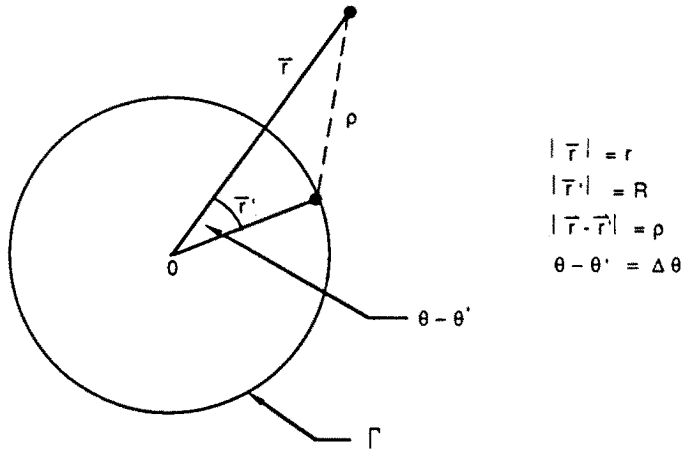

Figure 10 Scattering cross section calculation.

$$\chi(\theta) = \lim_{r\to\infty} 2\pi r \frac{|\bar{E}_S|^2}{|\bar{E}_i|^2} = \lim_{r\to\infty} 2\pi r \frac{|\bar{H}_S|^2}{|\bar{H}_i|^2} \tag{35}$$

which for either TM or TE waves can be written as

$$\chi(\theta) = \lim_{r\to\infty} 2\pi r |u_S|^2 \tag{36}$$

where we have assumed that $|u_i| = 1$ as it is, for example, in the case of a uniform plane wave.

Given u_S along the contour (see Fig. 10), we can calculate u_S at any exterior point from [14]

$$u_S(\bar{r}) = \int_\Gamma \left[G(\bar{r},\bar{r}') \frac{\partial u_S(\bar{r}')}{\partial n'} - \frac{\partial G(\bar{r},\bar{r}')}{\partial n'} u_S(\bar{r}') \right] dl' \tag{37}$$

where $G(\bar{r},\bar{r}') = \frac{1}{4j} H_0^{(2)}(\kappa\rho); \rho = |\bar{r} - \bar{r}'|$ is the outgoing free-space Green's function for the Helmholtz equation and $\partial/\partial n' = \partial/\partial R$. For large enough values of r the asymptotic form for the Hankel function gives the approximation

$$H_0^{(2)}(\kappa\rho) \sim \sqrt{\frac{2j}{\pi\kappa\rho}} e^{-j\kappa\rho} \sim \sqrt{\frac{2j}{\pi\kappa r}} e^{-j\kappa(r - R\cos\Delta\theta)} \tag{38}$$

where $\Delta\theta = \theta - \theta'$. Thus, for large r,

$$u_S(\bar{r}) \sim \frac{Rj}{4}\sqrt{\frac{2j}{\pi\kappa r}}e^{-j\kappa r}\int_0^{2\pi} F[u_S(\bar{r}')]e^{+j\kappa R\cos\Delta\theta}\,d\theta' \tag{39a}$$

with

$$F[u_S(\bar{r}')] = \left[\frac{\partial u_S(\bar{r}')}{\partial R} - (j\kappa\cos\Delta\theta)u_S(\bar{r}')\right] \tag{39b}$$

which leads to

$$\chi(\theta) = \frac{R^2}{4\kappa}\left|\int_0^{2\pi} F[u_S(\bar{r}')]e^{+j\kappa R\cos\Delta\theta}\,d\theta'\right|^2 \tag{39c}$$

Care must be exercised in performing the numerical integration since the integrand is highly oscillatory [24]. In the present work, we make the approximation

$$\int_0^{2\pi}\left[\frac{\partial u_S(\bar{r}')}{\partial R} - (j\kappa\cos\Delta\theta)u_S(\bar{r}')\right]e^{j\kappa R\cos\Delta\theta}\,d\theta' \approx$$

$$\sum_i\left\{\frac{\partial\overline{u_S^i}}{\partial R}\int_{\theta_i'}^{\theta_{i+1}'}\Psi(R,\Delta\theta)\,d\theta' - j\kappa\overline{u_S^i}\int_{\theta_i'}^{\theta_{i+1}'}\cos\Delta\theta\,\Psi(R,\Delta\theta)\,d\theta'\right\} \tag{40a}$$

with

$$\Psi(R,\Delta\theta) = e^{j\kappa R\cos\Delta\theta} \tag{40b}$$

where $\overline{u_S^i}$ is the average value of u_S over the i-th panel. Accurate values of $\partial u_S/\partial R$ can be obtained from flux balances along the outer contour. A linear approximation is then made to cos $\Delta\theta$ on each panel. The remaining integrals are then analytically evaluated. The resulting approximate expression for $\chi(\theta)$ takes the form of a discrete convolution and hence can be rapidly evaluated using FFT techniques.

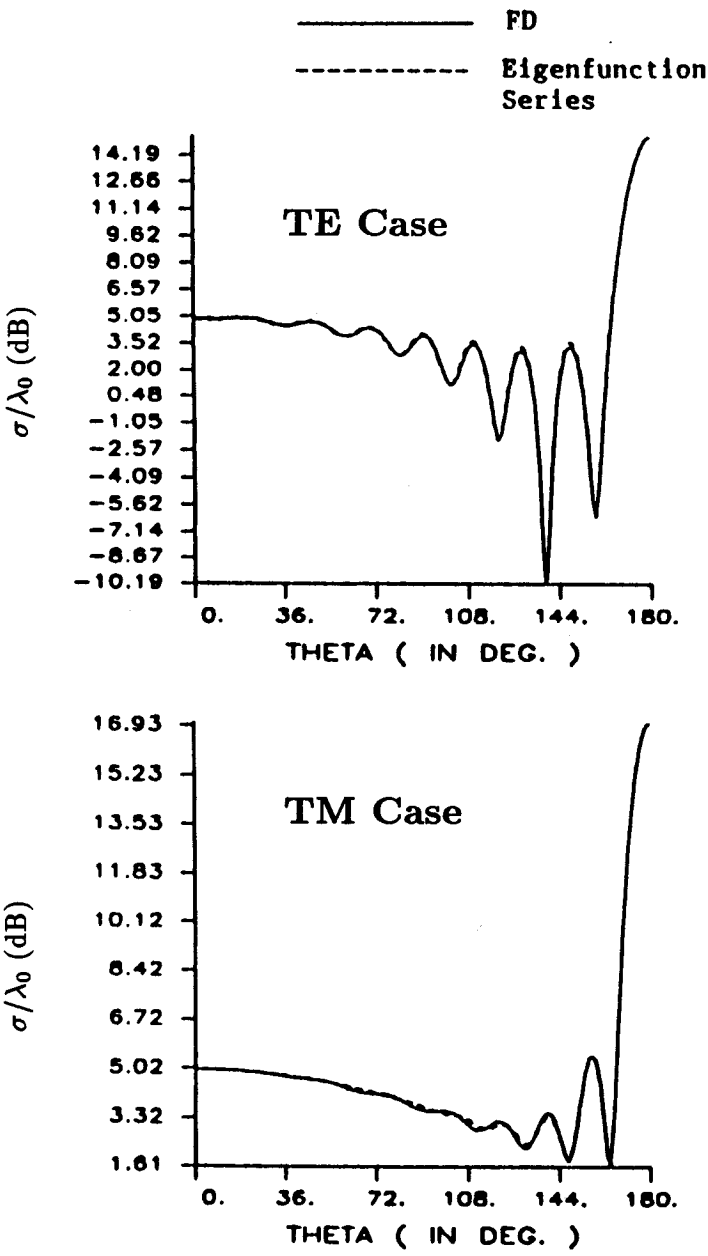

Figure 11 Bistatic patterns for a PEC circular cylinder ($k_0a = 10$). Outer computational boundary at $1.5a$.

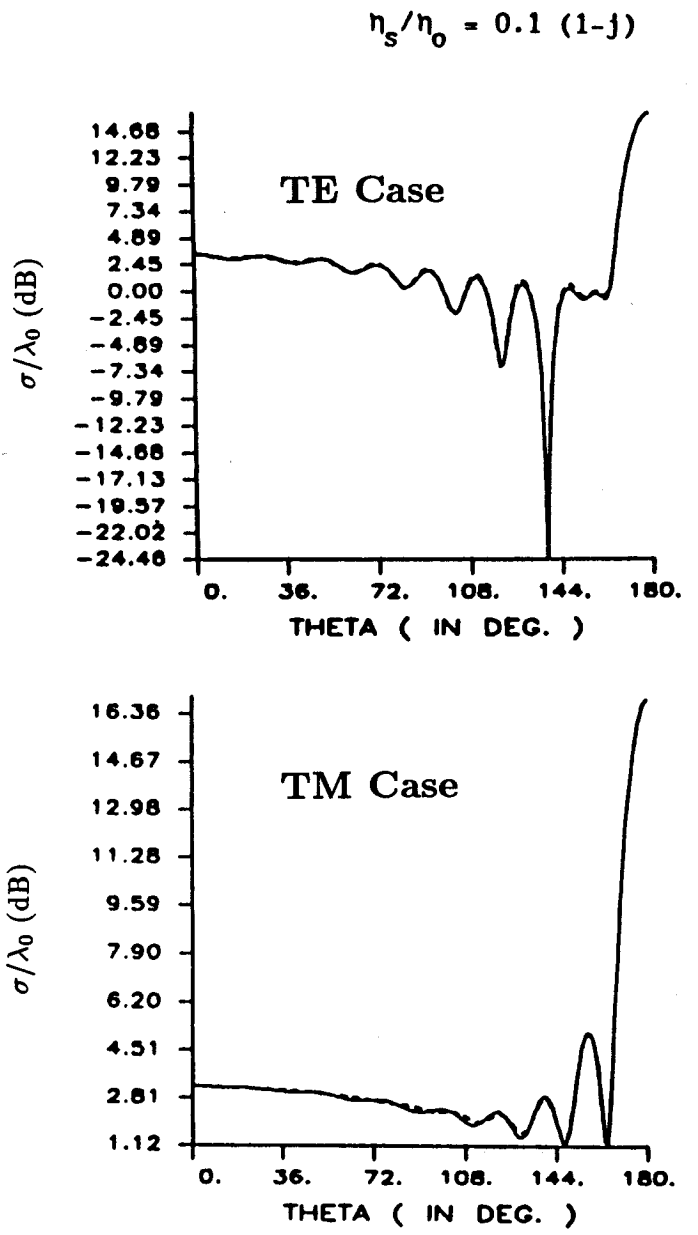

Figure 12 Bistatic patterns for an impedence sheet circular cylinder (k_0a= 10). (a) TE. (b) TM.

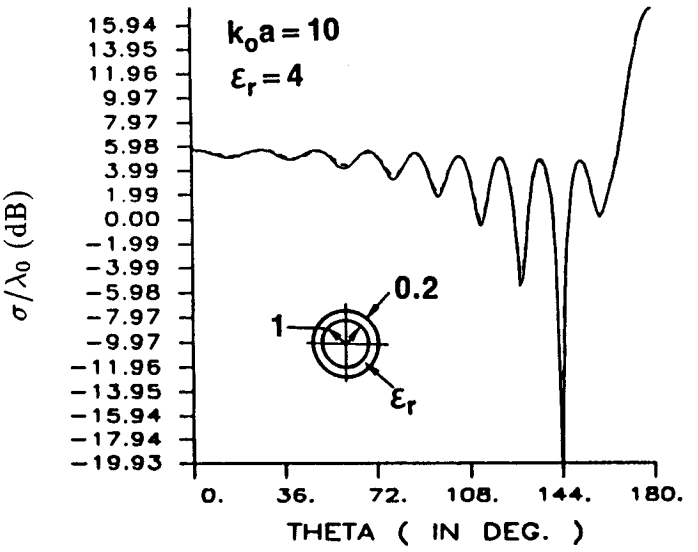

Figure 13 TE bistatic pattern for a dielectric clad PEC circular cylinder ($k_0a = 10$). Outer computational boundary at 1.5a. (a = radius of inner conductor).

5.7 Numerical Results

The generality and accuracy of using an asymptotic outer boundary condition with the control region finite difference formulation to solve two- dimensional scattering problems are illustrated in this section. The method is applied to a wide variety of targets, including smooth, perfectly electrically conducting (PEC) scatterers, objects with edges, coatings, thin films and cavities. The validity of the technique is examined by comparing the monostatic or bistatic cross sections, or the surface currents, with known solutions and measurements.

Highly accurate results were obtained for small and large PEC circular cylinders with dielectric coatings, impedance sheet claddings and axial slots. Figure 11 shows a comparison of the finite difference bistatic RCS results with the eigenfunction series expansion solutions for both TE and TM scattering. The radius, a, of the cylinder is $(10/2\pi)\lambda$ and the outer boundary condition is applied at 1.5 a, well within the Fresnel near zone of the scatterer. A polar mesh containing about 10,000 nodes was used in these examples. Excellent results were also obtained for a lossy impedance sheet cladding, Fig. 12, and a fairly

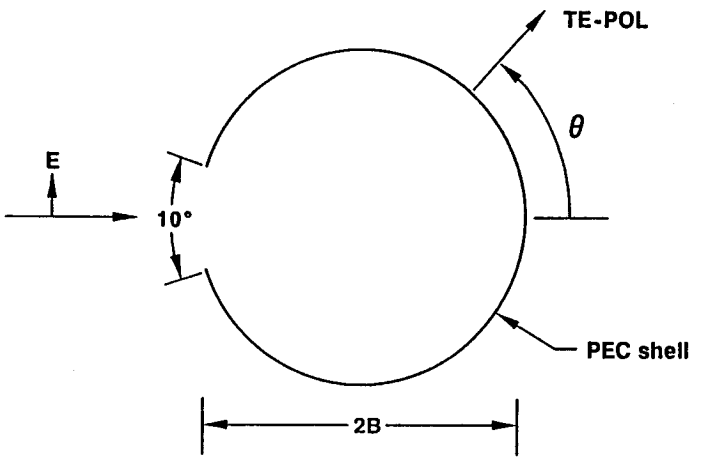

Figure 14 TE scattering from an axially slotted circular cylinder.

thick lossless dielectric layer, Fig. 13. The former case illustrates the use of the control region method to solve the wave equation with mixed interior boundary conditions. Dielectric coatings with large jumps in properties are also treated accurately as shown by the latter example.

An interesting use of the technique is to investigate the coupling between the scattered fields in a cavity-backed aperture (Fig. 14) and the currents on the exterior of the surrounding enclosure. If the Q of the cavity is large, that is if the coupling aperture is narrow, then the scattered fields will be extremely wavelength sensitive. In Fig. 15, we compare our results with the generalized dual series solutions obtained by Ziolkowski and Grant [25]. The solutions are in close agreement at both resonances and antiresonances which are extremely narrow. Finite difference and eigenfunction series solutions for the closed cylinder are also plotted for comparison.

The complete details of the near field are obtained without additional computation in our method. A contour plot of the scattered axial magnetic field (Fig. 16) at $k_0 B = \pi$ reveals the nature of the resonance in the monostatic cross section. The field pattern within the cavity is, apart from the values near the slot on the left-hand side of the figure, very nearly the same as the TE_{21} circular waveguide mode. It is clear that the effect of various types of wall loadings, posts and other obstacles within the cavity could be examined using the control region finite difference solution. Any shape of slot-coupled cylindrical cavity can be studied with this method.

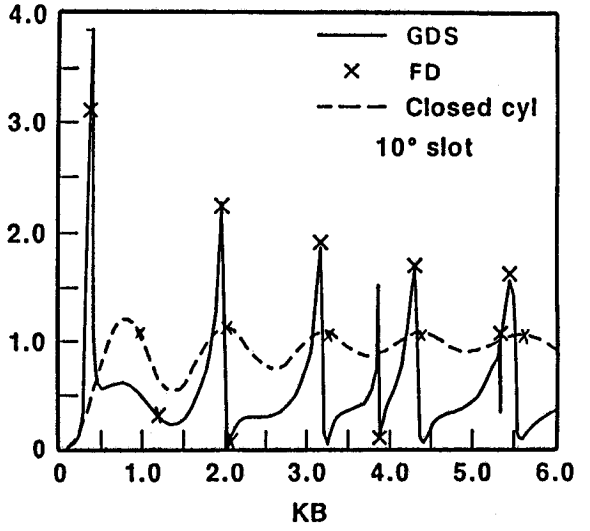

Figure 15 Normalized backscatter cross section ($\pi \cdot B$) of a cavity-backed axial slot in a cylinder [24].

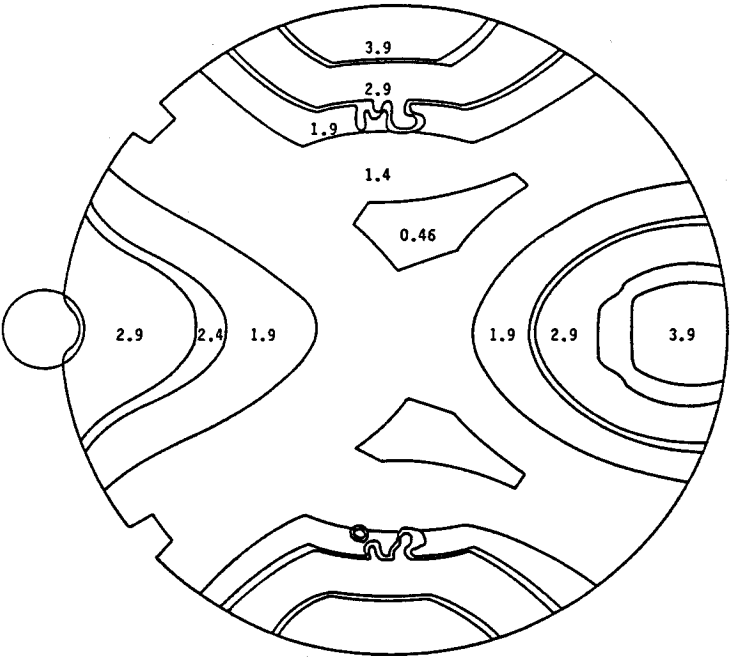

Figure 16 Scattered axial magnetic field strength contours for 10° slotted PEC cylinder ($k_0 B = \pi$). The slot is illuminated by a TE plane wave from 180°.

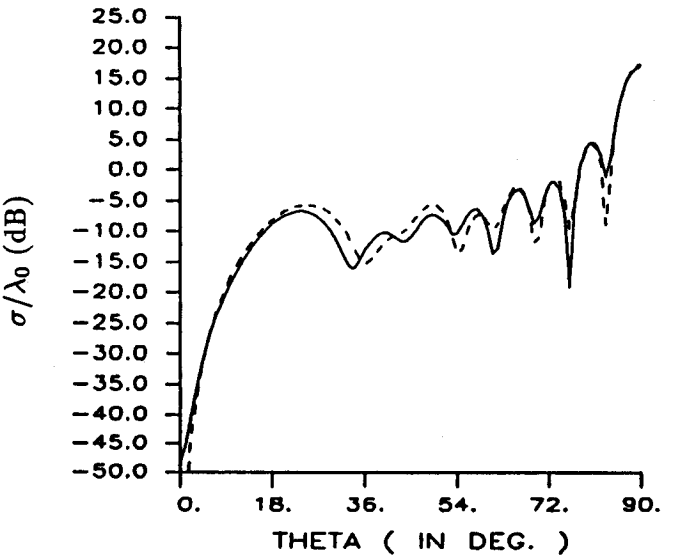

Figure 17 TE backscatter pattern from a PEC flat plate ($k_0W = 26.6$) computed using control region FD technique (———) and the approximate (— — —) Sommerfield-MacDonald expression [27].

The interaction between travelling waves and edges or joins, that have discontinuities in curvature, is another problem which can be investigated using the control region method. Here the capability of inspecting the near fields under conditions where travelling wave components are dominant can provide important insight as to the effect of lossy layers, variation in curvature, or surface impedance changes. TE scattering from a flat strip of width $(26.6/2\pi)\lambda$ (Fig. 17) shows a travelling wave lobe at 24°. A near field contour plot of the scattered $|H_z|$ field (Fig. 18) shows the buildup of the end-fire radiation and the standing wave formed by the incident and reflected components of the travelling wave excited by the 24° plane wave illumination. A lossy fairly thick (0.2λ) dielectric layer (Fig. 19) suppresses the travelling wave lobe, but increases the edge scattering. The outer computational boundary had a radius of 1.5ℓ where ℓ = half-length of strip and 10,000 mesh points were employed for these calculations.

Similar travelling wave interactions are also apparent in the illuminated side currents of a PEC square cylinder (Fig. 20). Note the excellent agreement between finite difference and method-of-moment results [26].

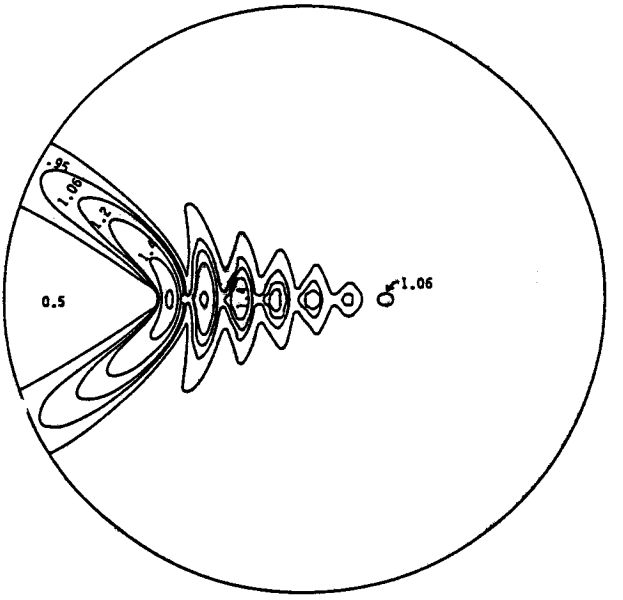

Figure 18 Contour plots of the scattered axial magnetic field strength for TE illumination of a PEC flat plate at $\theta = 24°$. Note the traveling wave interference pattern and the strong end-fire radiation.

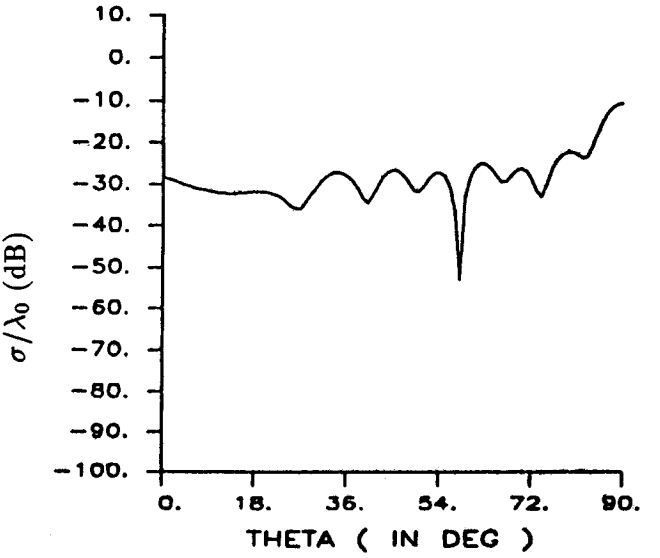

Figure 19 TE backscatter pattern for a lossy dielectric clad $t = 0.1a$ PEC plate ($k_0 a = 13.3$, $\epsilon_r = 2 + \mathrm{j}$).

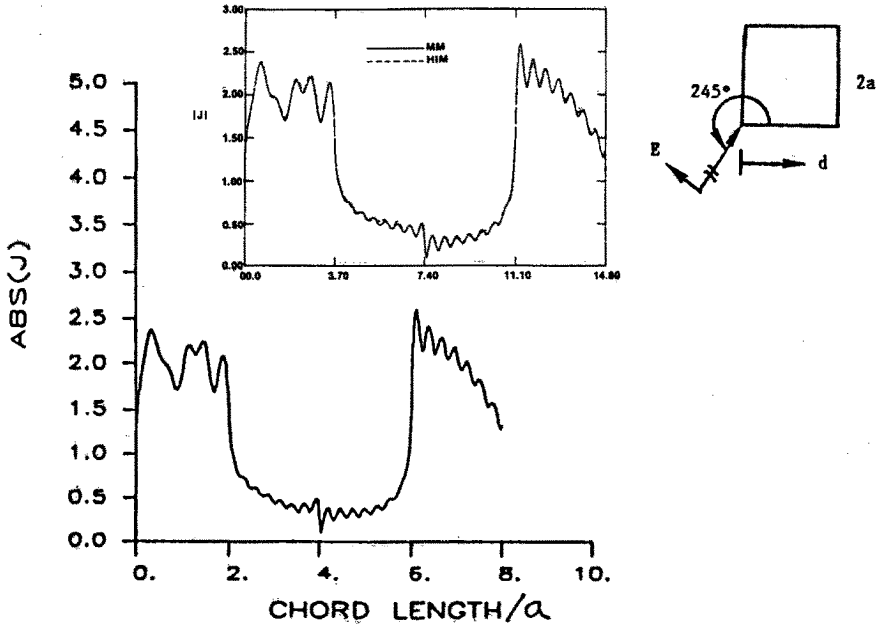

Figure 20 Magnitude of current on a square PEC cylinder illuminated by a TE plane wave at 245° ($k_0 a = 3.7\pi$). The graph in the insert is from Murthy, Hill, and Thiele [25].

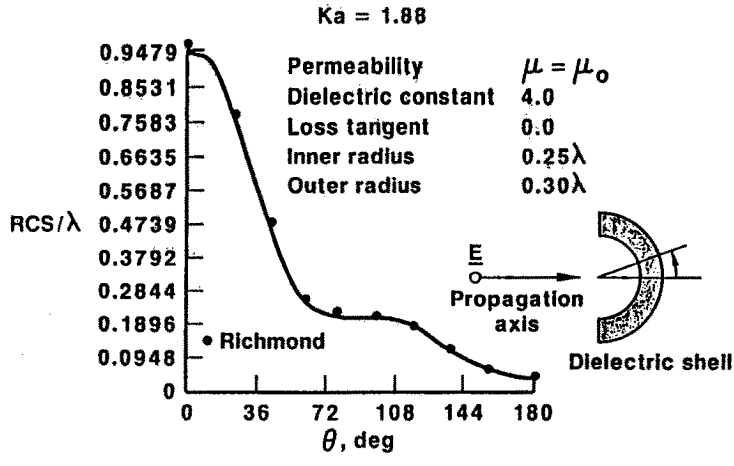

Figure 21 TM bistatic scattering pattern for a thin dielectric half-shell ($k_0 a = 1.88$) moment method results are from [26].

Scattering from curved dielectric shells and spar-shell airfoil shapes were also computed by the control region technique. Reentrant structures, similar to the dielectric shell, particularly those exhibiting strong multiple bounce returns are difficult to analyze by approximate methods. Results for the concave dielectric strip (Fig. 21) are in good agreement with the moment method solution obtained by Richmond [27].

Scattering from airfoil-section cylinders both PEC and dielectric layered were also investigated with our method. The airfoil contour (Fig. 22) is similar to the NACA series 65A shape (with $C_L = 0.532$). The TM bistatic patterns with incidence-illumination normal to the face, camber and edges of the airfoil are shown in Fig. 23. Good agreement (Table 1) is obtained with moment method results and measured values.

Table 1. Comparison of Measured and Computed RCS

Aspect	Airfoil RCS in DBSM		
	FD	MoM	Measured
TE	−13.2	−10.4	−7.6
Camber	9.9	12.3	11.8
LE	−11.8	−9.2	−7.0
Face	13.3	15.6	15.0

R_0 = FD outer boundary=1.6a, $k_0 a = 11.34$, a_0 = half-chord of airfoil.

TM scattering cross sections for a spar-shell airfoil (Fig. 23) are compared with measured values in Fig. 24. The outer radius of the boundary is at $1.5a$, where a is the semi-chord width. The outer shell has an $\epsilon = 4.2\epsilon_0$ and its thickness is 0.02λ. The spar is metal and the dielectric fill is lossless with $\epsilon = 1.28\epsilon_0$. The computed scattering widths were used to estimate the RCS of the 19 in. long experimental model by neglecting the scattering from the end caps. The cross section of the finite cylinder is approximated by

$$\sigma_{3D} \cong 8(h^2/\lambda) \cdot \sigma_{2D} \tag{41}$$

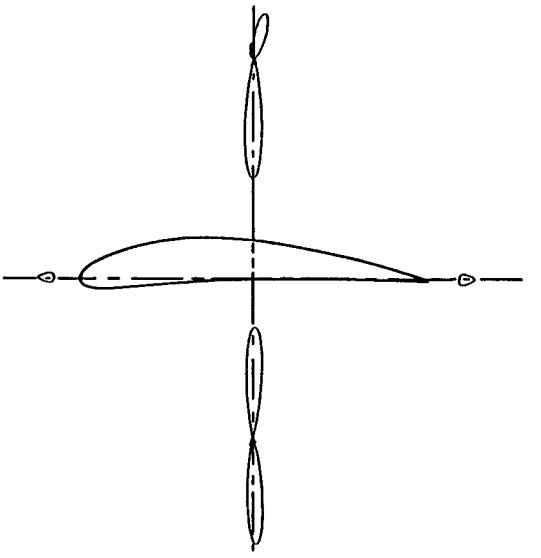

Figure 22 Bistatic cross section patterns for a PEC airfoil contour cylinder ($k_0 W = 22.68$).

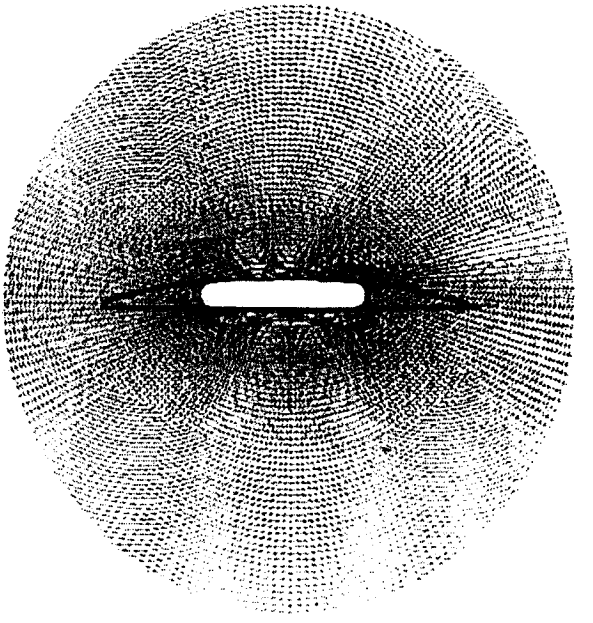

Figure 23 Spar-shell airfoil cylinder configuration.

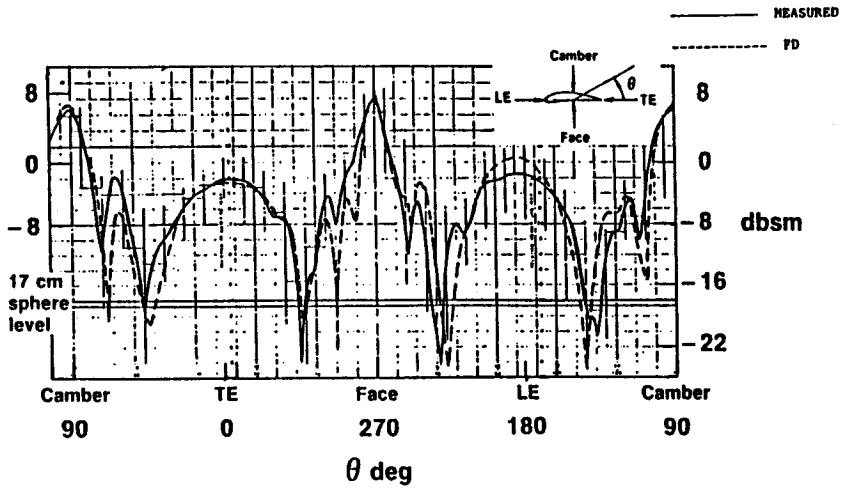

Figure 24 TM monostatic pattern of a spar-shell airfoil cylinder ($k_0W = 22.68$).

where $2h$ = cylinder length [28]. Results are shown for an airfoil with 3.5λ chord width. The differences between the computed and measured returns is probably ascribable to leading and trailing edge details of the airfoil which were not modeled in the analysis. Most of the features of the scattering pattern are quite accurately reproduced by the finite difference result. The overall agreement is seen to be quite good and reflects the useful engineering data obtainable from such a 2D finite differences analysis.

5.8 Conclusion

The preceding sections have shown by theoretical consideration and numerical examples that the Control Region Approximation combined with an outer asymptotic boundary condition provides a very powerful general tool for the analysis of electromagnetic scattering by complex targets. Accurate and efficient calculations of both near field quantities, such as surface currents, travelling waves, and cavity resonances, and far field quantities, such as monostatic and bistatic cross sections, are provided. We conclude with a consideration of improve-

ments to the two dimensional algorithm, extension to a three dimensional algorithm, and use of similar techniques for time-dependent scattering problems.

The two dimensional algorithm could be enhanced in a number of directions. Higher order discretizations are achievable by allowing the flux to vary along a Dirichlet edge. This would allow a reduction in mesh density. The outer boundary is presently circular. The use of more general outer contours, e.g. ellipses for long slender bodies, would permit a smaller computational domain and hence fewer mesh points. Finally, and perhaps most importantly, iteration of the right hand side of the outer asymptotic boundary condition may offer one possible way to sidestep our negative result pertaining to the use of higher order boundary conditions. Each iteration would be relatively inexpensive since only the source terms would change.

Extension of the algorithm to three dimensions (3D) is a complex multi-faceted problem. There are a number of choices for a suitable formulation of the governing equations and the asymptotic boundary condition. Recent results [17,29] for specialized bodies of revolution, using a pair of scalar potentials to represent the field [30], appear promising. Asymptotic boundary conditions, analogous to Bayliss-Turkel, can also be derived for the 3D vector problem [31]. Algorithms to provide Dirichlet/Delaunay tessellations in three dimensions must be constructed. Furthermore, since the 3D formulation may not lead only to divergence operators, shear terms as well as the usual flux terms must be dealt with on the boundaries of the Dirichlet boxes. Finally, the sheer number of equations resulting from discretizing a region of space as well as from treating a vector problem will likely make the computational needs of present sparse matrix solvers very intensive. Utilization of parallel algorithms and architectures will almost certainly be necessary for large targets.

The use of time-marching algorithms for electromagnetics problems has heretofore been rather limited. Most previous work has been restricted to Cartesian grids with their attendant limitations. However, in areas such as computational fluid dynamics, time marching is standard fare in both 2D and 3D. The Dirichlet/Delaunay duality can be utilized to make the spatial discretization provided by the Control Region Approximation compatible with many of the standard time-marching schemes such as the Lax-Wendroff method.

In summary, the Control Region Approximation provides a new and powerful approach to solving for electromagnetic scattering from

complex inhomogeneous targets. The method is completely general in that it can accommodate scatterers of arbitrary shape and composition while incorporating a physical model which includes all scattering mechanisms. The sparse structure of the discrete model allows economical use of computer resources.

Acknowledgements

The authors would like to acknowledge several illuminating discussions with Prof. Raj Mittra of the University of Illinois at Urbana-Champaign. The cooperation of Prof. Andrew Peterson, also of the University of Illinois, in providing moment method computations for the PEC airfoil is greatly appreciated. They would also like to express their gratitude for the support and encouragement of the Sikorsky Aircraft and Advanced Systems Divisions of United Technologies. The extensive editorial comments of Dr. Joseph R. Caspar of UTRC are felt to have greatly improved the quality of presentation in this paper.

References

[1] Keller, J. B., "Geometrical theory of diffraction," *J. Opt. Soc. Am.*, **52**, 116–130, 1962.

[2] Harrington, R. F., *Field Computation by Moment Methods*, Krieger, 1985.

[3] Engquist, B., and A. Majda, "Absorbing boundary conditions for the numerical simulation of waves," *Math. Comp.*, **31**, 629–651, 1977.

[4] Bayliss, A., and E. Turkel, "Radiation boundary conditions for wave-like equations," *Comm. Pure and Appl. Math.*, **33**, 707–725, 1980.

[5] Caspar, J. R., D. E. Hobbs, and R. L. Davis, "Calculation of two-dimensional potential cascade flow using finite area methods," *AIAA J.*, **18**, 103–109, 1980.

[6] McCartin, B. J., J. R. Caspar, R. E. LaBarre, G. A. Peterson, and R. H. Hobbs, "Steady state numerical analysis of single carrier two-dimensional semiconductor devices using the control area ap-

proximation," *NASECODE III Proceedings*, J. J. H. Miller (Ed.), Boole Press, 185–190, 1983.

[7] McCartin, B. J., "Solution of complex Helmholtz equations in arbitrary geometries," *SIAM Nat. Mtg.*, Boston, MA, July 24, 1986.

[8] McCartin, B. J., "Discretization of the semiconductor device equations," *New Problems and New Solutions for Device and Process Modelling*, Boole Press, 72–80, 1985.

[9] Eisenstat, S. C., M. C. Gursky, M. H. Schultz, and A. H. Sherman, Yale Sparse Matrix Package I. The Symmetric Codes, Yale U. Dept. of Comp. Sci. RR#112.

[10] Zienkiewicz, O. C., and Y. K. Cheung, "Finite elements in the solution of field problems," *The Engineer*, 507–510, 1985.

[11] Eisenstat, S. C., M. C. Gursky, M. H. Schultz, and A. H. Sherman, Yale Sparse Matrix Package II. The Nonsymmetric Codes, Yale U. Dept. of Comp. Sci. RR#114.

[12] Kong, J. A., *Electromagnetic Wave Theory*, Wiley, 1986.

[13] Wang, D. S., "Limits and validity of the impedance boundary condition on penetrable surfaces," *IEEE Trans. Antennas Propagat.*, **AP-35**, 453–457, 1987.

[14] Baker, B.B., and E.T. Copson, *The Mathematical Theory of Huyghen's Principle*, Chelsea, 1987.

[15] Trefethen, L. N., "Well-posedness of one-way wave equations and absorbing boundary conditions," *ICASE* Report No. 85–30, 1985.

[16] Hariharan, S. I., "Absorbing boundary conditions for exterior boundary value problems," *ICASE* Report No. 85–33, 1985.

[17] Mittra, R., O. Ramahi, G. Meltz, and B. J. McCartin, "A new look at the asymptotic boundary conditions for differential equation approaches to solving open region scattering problems," *Proc. 1987 URSI Radio Sci. Mtg.*, p. 251.

[18] IMSL Library Reference Manual, Edition 9, Volume 2, Chapter I, IRATCU 1–4, Houston, TX, 1983.

[19] Dirichlet, G. L., "Über die reduction der positiven quadratischen formen mit drei unbestimmten ganzen zahlen," *Z. Reine Angew. Math.*, **40**, 209–227, 1850.

[20] Delaunay, B., "Sur la sphere vide," Bull. Sci. USSR (VII), *Classe Sci., Mat. Nat.*, 793–800, 1934.

[21] Watson, D. F., "Computing the N-dimensional Delaunay tessellation with applications to Voronoi polytopes," *Comp. J.*, **24**, 167–172, 1981.

[22] McCartin, B. J., "Alternative basis functions using Green's functions," in preparation – contact authors for updated citation.

[23] Birkhoff, G., and R. E. Lynch, *Numerical Solution of Elliptic Problems,* SIAM, 1984.

[24] Davis, P. J., and P. Rabinowitz, *Methods of Numerical Integration,* Academic Press, 1975.

[25] Ziolkowski, R. W., and J. B. Grant, "Scattering from cavity-backed apertures: The generalized dual series solution of the concentrically loaded E-pol slit cylinder problem," *IEEE Trans. Antennas Propagat.*, **AP-35**, 504–528, 1987.

[26] Murthy, P. K., K. C. Hill, and G. A. Thiele, "A hybrid-iterative method for scattering problems," *IEEE Trans. Antennas Propagat.*, **AP-34**, 1986.

[27] Richmond, J. H., "Scattering by a dielectric cylinder of arbitrary cross section shape," *IEEE Trans. Antennas Propagat.*, **AP-13**, 1965.

[28] Ruck, G. T., *Radar Cross Section Handbook*, **2**, 499–504, Plenum Press, New York, 1970.

[29] Mittra, R., and O. Ramahi, "Absorbing boundary conditions for the direct solution of partial differential equations arising in electromagnetic scattering problems," this text, Chapter 4.

[30] Morgan, M. A., and K. K. Mei, "Finite element computation of scattering by inhomogeneous penetrable bodies of revolution," *IEEE Trans. Antennas Propagat.*, **AP-27**, 202–214, 1979.

[31] Wilcox, C. H. "An expansion theorem for electromagnetic fields," *Comm. Pure and Appl. Math.,* **IX**, 115–134, 1956.